Mueller matrix polarimetry for differentiating characteristic features of cancerous tissues

E Du
Honghui He
Nan Zeng
Minghao Sun
Yihong Guo
Jian Wu
Shaoxiong Liu
Hui Ma

Mueller matrix polarimetry for differentiating characteristic features of cancerous tissues

E Du,[a,b] Honghui He,[b] Nan Zeng,[b] Minghao Sun,[a,b] Yihong Guo,[a,b] Jian Wu,[b] Shaoxiong Liu,[c] and Hui Ma[a,b,*]
[a]Tsinghua University, Department of Physics, Beijing 100084, China
[b]Tsinghua University, Graduate School at Shenzhen, Shenzhen Key Laboratory for Minimal Invasive Medical Technologies, Shenzhen 518055, China
[c]Huazhong University of Science and Technology Union Shenzhen Hospital, Shenzhen Sixth People's Hospital (Nanshan Hospital), Shenzhen 518052, China

Abstract. Polarization measurements allow one to enhance the imaging contrast of superficial tissues and obtain new polarization sensitive parameters for better descriptions of the micro- and macro- structural and optical properties of complex tissues. Since the majority of cancers originate in the epithelial layer, probing the morphological and pathological changes in the superficial tissues using an expended parameter set with improved contrast will assist in early clinical detection of cancers. We carry out Mueller matrix imaging on different cancerous tissues to look for cancer specific features. Using proper scattering models and Monte Carlo simulations, we examine the relationship between the microstructures of the samples, which are represented by the parameters of the scattering model and the characteristic features of the Mueller matrix. This study gives new clues on the contrast mechanisms of polarization sensitive measurements for different cancers and may provide new diagnostic techniques for clinical applications. © 2014 Society of Photo-Optical Instrumentation Engineers (SPIE) [DOI: 10.1117/1.JBO.19.7.076013]

1 Introduction

In recent years, various polarization techniques have been developed and tested for different clinical applications, especially for cancer detections.[1–3] It has been demonstrated that the simple linear degree of polarization (LDOP) imaging can mark the margins of cancerous tissues in both *ex vivo* and *in vivo* conditions.[4–6] Since the LDOP imaging of anisotropic tissues can be sensitive to the orientation of the samples,[7] a rotating linear polarization imaging (RLPI) method has been developed to provide a set of orientation insensitive parameters, which can be used to differentiate different microstructural features in cancerous tissues.[8–11] Mueller matrix imaging methods were also tested in various clinical applications.[12–14] However, although it comprehensively describes how the polarization states are transformed from the incident into the scattered light, a Mueller matrix reveals limited explicit information on the structural or optical properties of the medium. To address this problem, different Mueller matrix decomposition techniques have been proposed, which derive a set of polarization parameters with specific physical meanings, such as the diattenuation D, retardance R, and depolarization power Δ obtained by the Mueller matrix polar decomposition (MMPD).[15–17] Inspired by RLPI, a Mueller matrix transformation (MMT) technique was also proposed to derive new polarization parameters, which are functions of the Mueller matrix elements but are explicitly correlated to specific microstructures or the optical properties of the medium, such as the densities and sizes of subwavelength scatterers or the orientation and alignment of the fibers.[18] These different polarization techniques rely on different contrast mechanisms and have their own advantages and disadvantages.

In this paper, we compare three different polarization imaging methods: LDOP, MMPD, and MMT using two cancerous tissues of different microstructures, such as human basal cell carcinoma (BCC) and papillary thyroid carcinoma. Then, using Monte Carlo simulations based on a sphere-cylinder birefringence scattering model (SCBM)[19–22] that approximates the anisotropic biological tissues to a mixture of spherical and cylindrical scatterers imbedded in a birefringent ambient medium, we examine the relationship between the polarization imaging parameters and the morphological and pathological features in the cancerous tissues. The simulations and experiments provide new clues on the contrast mechanisms of various polarization imaging techniques for cancerous tissues.

2 Method and Materials

2.1 Sample and Experimental Setup

Figure 1 shows the typical experimental setup for the backscattering Mueller matrix measurements.[22] The light source is a 3 W LED with a center wavelength of 650 nm. The light beam passes through a linear polarizer (P1) and a quarter-wave plate (QW1) to generate six different polarization states: horizontal linear (H), vertical linear (V), 45-degree linear (P), 135-degree linear (M), right circular (R), and left circular (L). The incident beam illuminates the sample at about 20 deg to the normal to reduce surface reflection. The backscattered light from the sample passes through the analyzer, which consists of a quarter-wave plate (QW2) and a polarizer (P2), and is collected by an
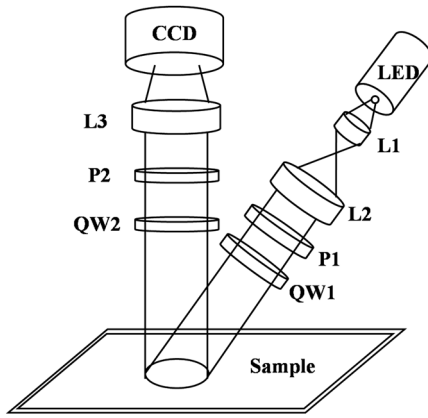
Fig. 1 Schematic of experimental setup for the backscattering Mueller matrix measurement. L, lens; P, polarizer; QW, quarter-wave plate. The LED light source illuminates the sample at about 20 deg to the normal to eliminate the surface reflection. The diameter of the illumination area is about 2 cm.

8-bit charge coupled device camera. For each incident state, six polarization components (H, V, P, M, R, and L) are measured. Then, the backscattering Mueller matrix can be calculated from the 36 images.[22] During the experiments, we defined a reference coordinate system whose horizontal direction (H) is parallel to the plane defined by the source-sample-camera triangle. Before being applied to tissue samples, the experimental setup was first calibrated by measuring the backscattering Mueller matrix of standard samples such as microsphere solutions. The results demonstrate that the errors for all the measured Mueller matrix elements are less than 3%.

Once the Mueller matrices are obtained, polarization properties of the samples can be represented by different parameters, all of which are expressed as functions of the Mueller matrix elements. In this paper, we use polarization parameters from three different techniques: LDOP, MMPD, and MMT. For LDOP, it can be calculated as in Eq. (1):[5]

$$\text{LDOP} = \frac{I_{\text{par}} - I_{\text{per}}}{I_{\text{par}} + I_{\text{per}}} = \frac{\text{HH} - \text{HV}}{\text{HH} + \text{HV}} = \frac{\text{m21} + \text{m22}}{\text{m11} + \text{m12}}, \tag{1}$$

where I_{par} and I_{per} represent the polarization components with the analyzer parallel or perpendicular to the polarization state of the incident light, and HH and HV represent the polarization components corresponding to horizontal incident polarization (the first capital H) and horizontal or vertical detection polarization (the second capital H or V). As shown in Eq. (1), the LDOP can also be calculated directly using the Mueller matrix elements m11, m12, m21, and m22. For the MMPD proposed by Lu and Chipman,[15] the Mueller matrix is decomposed into a product of three submatrices: depolarization (M_Δ), retardance (M_R), and diattenuation (M_D) as shown as Eq. (2),

$$M = M_\Delta \cdot M_R \cdot M_D. \tag{2}$$

A set of parameters are derived corresponding to these matrices, i.e., the depolarization power Δ, the retardance R (including the linear retardance δ and circle retardance Ψ), and the diattenuation D.[15] For the MMT, we use a set of parameters that are explicitly related to different characteristic microstructures of the anisotropic tissue samples, such as the density of subwavelength scattering particles or the orientation and alignment of the fibrous structures.[18] The MMT parameters b and A can be expressed as Eq. (3):[18]

$$b = \frac{\text{m22} + \text{m33}}{2}$$

$$A = \frac{2 \cdot (\text{m22} + \text{m33}) \cdot \sqrt{(\text{m22} - \text{m33})^2 + (\text{m23} + \text{m32})^2}}{(\text{m22} + \text{m33})^2 + (\text{m22} - \text{m33})^2 + (\text{m23} + \text{m32})^2}$$

$$\in [0,1].$$

$$\tag{3}$$

All the human cancerous samples used in this study are provided by Shenzhen Sixth People's (Nanshan) Hospital. After surgery, the human cancerous tissue samples are cut into pieces a few millimeters thick, fixed in formalin, dehydrated, and embedded in paraffin. Then, the nonstained paraffin slices of about a 28-μm thickness are prepared with a microtome and imaged using the backscattering Mueller matrix imaging method. Following standard pathology procedures, the 4-μm thick paraffin slices are cut from the same paraffin block, rehydrated, and stained with hematoxylin-eosin (H-E) to make the histological plates. We compare the polarization images of the nonstained 28-μm thick slices with the microscope images of the H-E stained 4-μm thick slices.
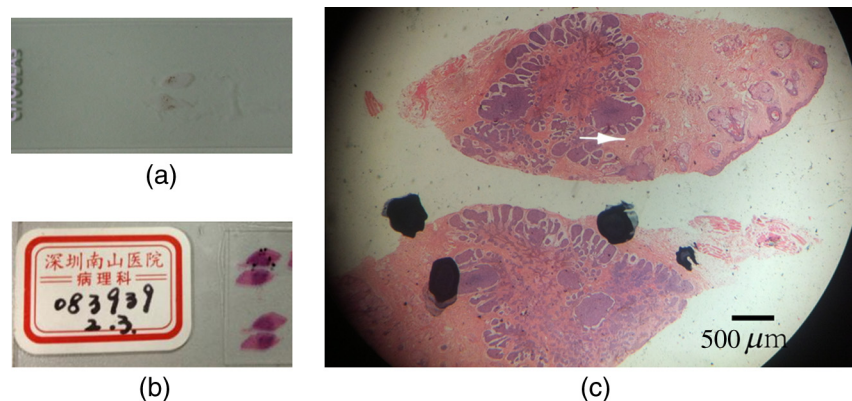

Fig. 2 (a) Photograph of a 28-μm thick nonstained paraffin slice of human skin basal cell carcinoma (BCC) tissues and the size of the sample is about 0.5 cm, (b) photograph of the corresponding 4-μm thick H-E stained paraffin slice of the BCC tissue, (c) microscope image of the H-E stained paraffin slice of the BCC tissue, the darker regions are cancerous tissues.

Figures 2(a) and 2(b) show the images of a nonstained 28-μm thick paraffin slice and the corresponding H-E stained 4-μm thick paraffin slice of human skin BCC. The microscope image of the H-E stained slice [Fig. 2(c)] shows that there are two dysplastic regions where the stained colors are darker than that of the healthy tissues. Pathological diagnosis identified that the dysplastic regions are BCC tissues. Figures 3(a) and 3(b) show the images of a nonstained 28-μm thick paraffin slice and the corresponding H-E stained 4-μm thick paraffin slice of a papillary thyroid carcinoma (PTC). The size of the PTC sample is much larger than that of the BCC sample. We examined the microscope image of the H-E stained PTC tissues and found that there are circularly aligned fibers around the cancerous tissues. Figure 3(c) shows the microscope image of the black square marked region of the H-E stained PTC tissues [Fig. 3(b)]. Pathological diagnosis identified that the tissues in the left part of Fig. 3(c) are fibers and the tissues in the right part are cancerous tissues. Figure 3(d) shows the microscope image of the red square marked region of the H-E stained PTC tissue [Fig. 3(b)]. The tissues in the left part of Fig. 3(d) are cancerous tissues and the tissues in the right part are fibers.

2.2 Monte Carlo Simulation

In previous works, we have developed a SCBM[19–21] and a corresponding Monte Carlo simulation program, which tracks the trajectories and polarization states of scattered photons. SCBM contains three key components: spherical scatterers, cylindrical scatterers, and a birefringent ambient medium, mimicking the microscopic structures and optical properties of tissues. For example, the cell nuclei or organelles can be simulated as the spherical scatterers, and the fibers can be approximated as cylindrical scatterers. In the Monte Carlo program, the refractive indices, the scattering coefficients, and the radius of both the spheres and cylinders, together with the orientation and angular distribution of the cylinders can be adjusted. For the ambient medium, the refractive index, the absorption coefficient, the optical activity coefficient, and the value and direction of

birefringence are variables. In this paper, the parameters of the simulations are set according to the characteristic features of different tissues, and will be introduced in the following sections.

3 Results and Discussions

First, we measured the backscattering Mueller matrix of the nonstained 28-μm thick paraffin slice of BCC sample shown in Fig. 2(a), which does not exhibit distinctive structures under either transmission or reflection microscopes. Figure 4 shows the backscattering Mueller matrix of the nonstained paraffin slice. It can be observed that the Mueller matrix elements of the BCC sample have diagonal symmetry. The nondiagonal Mueller matrix elements are all close to zero, showing that the BCC samples are close to isotropic. The intensity of the m22 element is almost the same as that of the m33 element (m22 = m33). The intensity of the m44 element is smaller than the intensities of the m22 and m33 elements (m44 < m22 = m33).

From the images of the Mueller matrix elements, we can calculate the images of other polarization parameters pixel by pixel including the LDOP, MMT parameters b and A, MMPD parameters diattenuation D, depolarization power Δ, and linear retardance δ as shown in Fig. 5. The experimental results clearly show that for the BCC sample, the linear retardance δ and the anisotropy A are all close to zero. This is proof that the human BCC skin tissues are highly isotropic. $A = 0$ indicates that the sample does not contain aligned fibrous scatterers,[18] while $\delta = 0$ means that there are neither aligned fibers nor a birefringent interscatterer ambient medium.[21] Figure 5 shows that the depolarization is the dominate effect in the BCC samples. Meanwhile, the LDOP, b, D and Δ images clearly represent two regions which are similar to the cancerous areas shown in the microscopic view of the H-E stained slice [Fig. 2(c)].

In the cancerous regions on the BCC sample, the values of the LDOP, b, and D are larger than those in the normal regions, while the values of Δ are smaller. According to Eqs. (1) and (3),
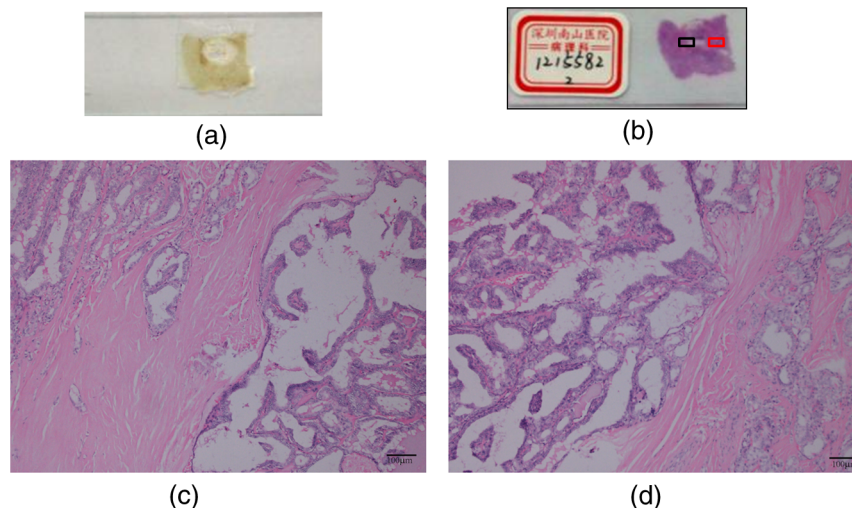

(a)

(b)

(c)

(d)

Fig. 3 (a) Photograph of a 28-μm thick nonstained paraffin slice of human papillary thyroid carcinoma (PTC) tissues and the size of the sample is about 2 cm, (b) photograph of the corresponding 4-μm thick H-E stained paraffin slice of the PTC tissue, (c) microscope image of the black square marked region of H-E stained paraffin slice of the PTC tissue. The tissues in the left part are fibers and the tissues in the right part are cancerous tissues, (d) microscope image of the red square marked region of H-E stained paraffin slice of the PTC tissue. The left tissues are cancerous tissues and the right tissues are fibers.
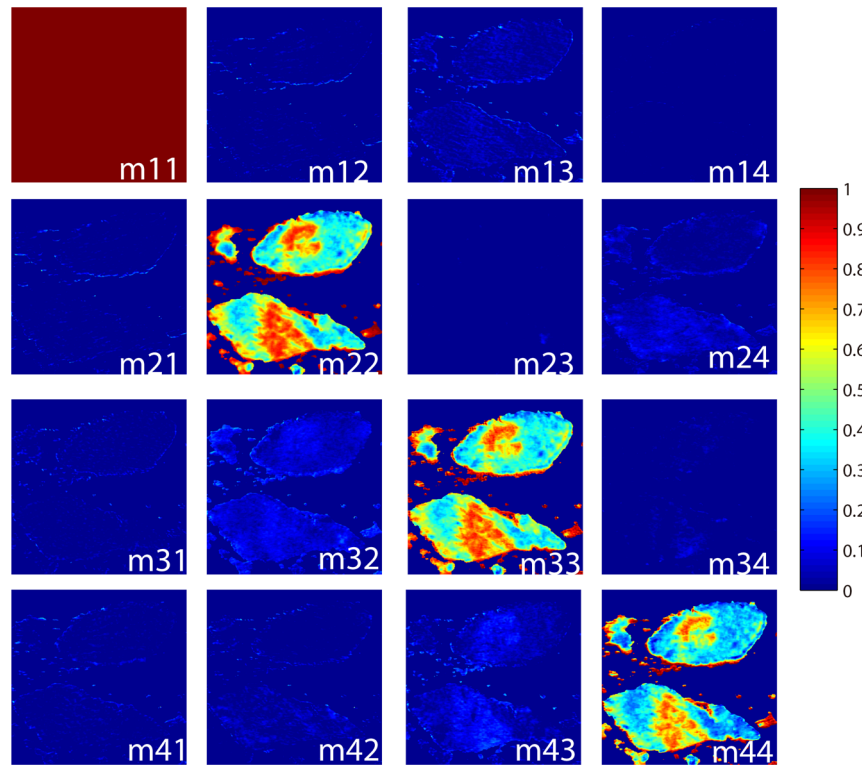
Fig. 4 Normalized backscattering Mueller matrix of a 28-μm thick nonstained paraffin slices of the BCC skin tissues shown in Fig. 2(a). All the Mueller matrix elements are normalized by the m11. The color codes are from 0 to 1 for all the elements.
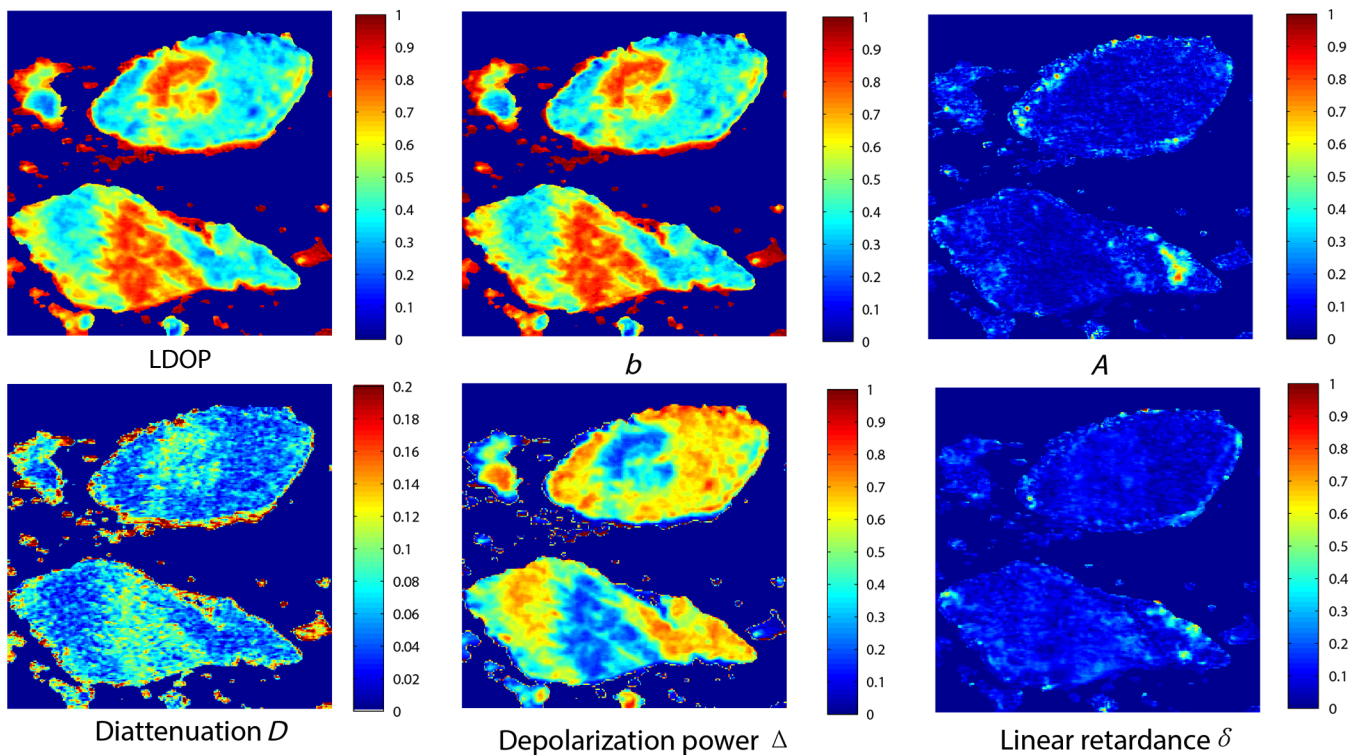

Fig. 5 Two-dimensional images of the polarization parameters of BCC skin tissues shown in Fig. 2(a): LDOP, MMT parameters b, A, MMPD parameters diattenuation D, depolarization power Δ and linear retardance δ.

for isotropic samples the values of both the LDOP and MMT parameter b are equal to the m22 or m33 elements (LDOP = b = m22 = m33). Since the m22 and m33 elements are correlated to the linear-polarization maintaining power of the scattering media, LDOP and b also represent the linear-polarization maintaining capability. Parameter Δ reflects the depolarization power for linear and circular incident polarization states. The experimental results show that the cancerous tissues are less depolarizing than healthy tissues. Comparisons between microscope images of the H-E stained slices and polarization images of the nonstained slices confirm that the polarization images for the parameters LDOP, b, D, and Δ can be used to distinguish cancerous and normal regions for isotropic BCC tissues.

To examine the contrast mechanisms of the polarization images, we conduct Monte Carlo simulations based on the SCBM and investigate the relationship between the parameters of the observed polarization and the parameters of the scattering model, which represent the microstructures of the tissues. For the 28-μm thick skin samples, we use a single-layered model to mimic the epidermis tissues.[20] Since the BCC samples are isotropic, the density of cylindrical scatterers and birefringence of the ambient medium are set to zero. The scattering model for BCC consists of spherical scatterers with two different sizes: the "large" ones (4 μm in radius) represent the cell nuclei (2.5–5 μm in radius), the "small" ones (0.25 μm in radius) represent the cell organelles (a few hundred nanometers in diameter) such as mitochondria, lysosomes, and ribosomes. The refractive indices of both spherical scatterers are set to 1.45 according to Ref. 23. The refractive index of the ambient media is 1.33. The microscope images of the H-E stained skin BCC tissues have shown that both the cellular densities and sizes of the nuclei increase for cancerous cells. Therefore, in simulations, we enlarge the "large" spherical scatterers and increase the densities of both the "large" and "small" spherical scatterers to examine how such cancer specific structural features affect the polarization imaging parameters. First, we keep the density of the spherical scatterers constant and increase the radius of the "large" scatterers from 4 to 8 μm. As shown in Fig. 6(a), as the size of the "large" scatterers increases, both the LDOP and b decrease, while Δ stays almost unchanged. Then, we fix the radius of the spherical scatterers and increase the scattering coefficient of the "large" scatterers from 0 to 400 cm^{-1}. Monte Carlo simulated results in Fig. 6(b) demonstrate that both the LDOP and b decrease and the depolarization power Δ increases with the increasing scattering coefficient of the "large" scatterers. The simulated results show that only Fig. 6(c) fits the experimental observations of the BCC sample where the LDOP and b increase but Δ decreases in the cancerous regions. Such quantitative agreement between the experiments and simulations indicates that for the BCC tissues, the dominant contrast mechanism for polarization measurements is the increased number density of the "small" scatterers or the cell organelles. For cancerous tissues, the well-known pathological features include increases in the cell density and number density of the mitochondria, both of which lead to increases in the number of "small" scatterers in the cancerous region.[1]

We also applied polarization measurements to the nonstained paraffin slices of human PTC tissues. We measured the 28-μm thick nonstained paraffin slice of PTC tissue [shown in Fig. 3(a)]. The normalized backscattering Mueller matrix of the sample is shown in Fig. 7. It can be observed that unlike the BCC tissues, the nondiagonal Mueller matrix elements of
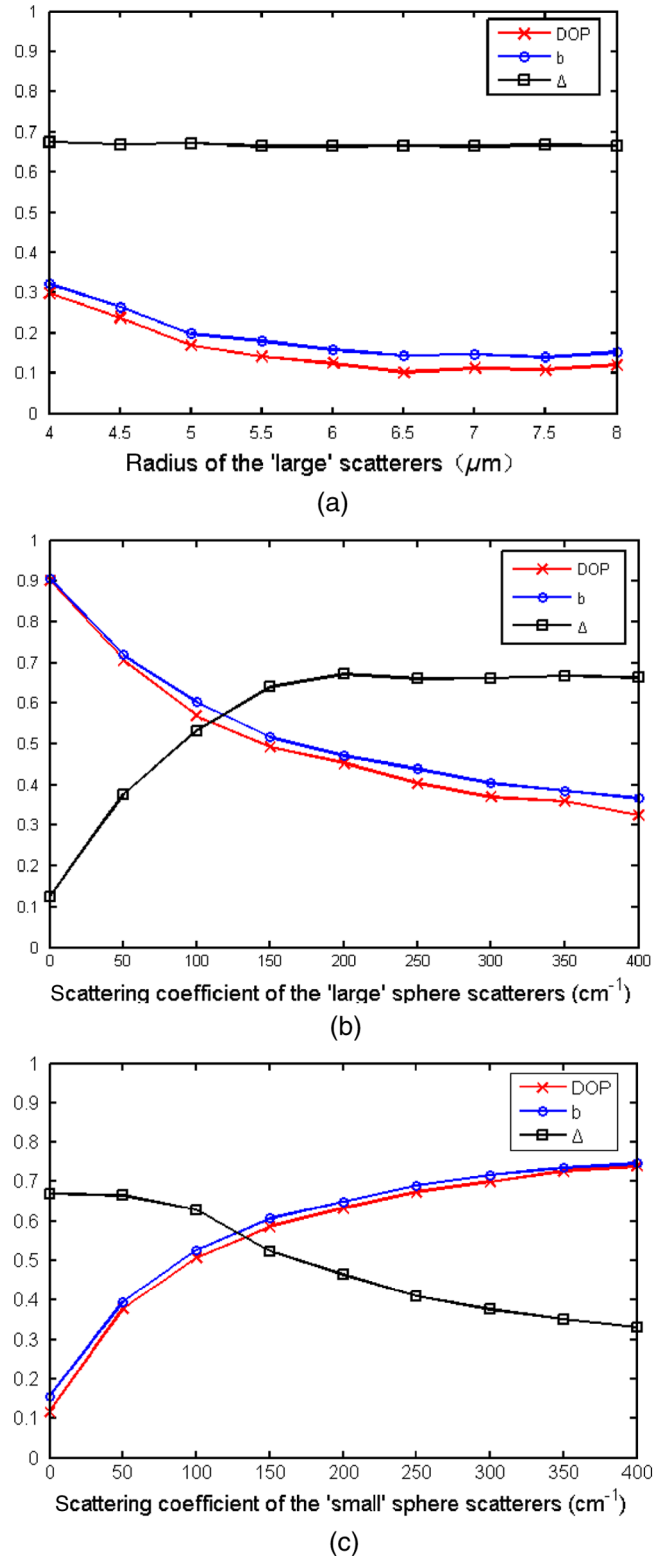

(a)

(b)

(c)

Fig. 6 Monte Carlo simulated parameters LDOP, b, and Δ as functions of (a) the radius of the "large" scatterers, (b) the scattering coefficient of the "large" scatterers and (c) the scattering coefficient of the "small" scatterers.

the PTC tissues are not close to zero, which indicates the thyroid tissues are anisotropic.[24]

Using the normalized backscattering Mueller matrix images of the PTC tissues, we calculated the images of the polarization
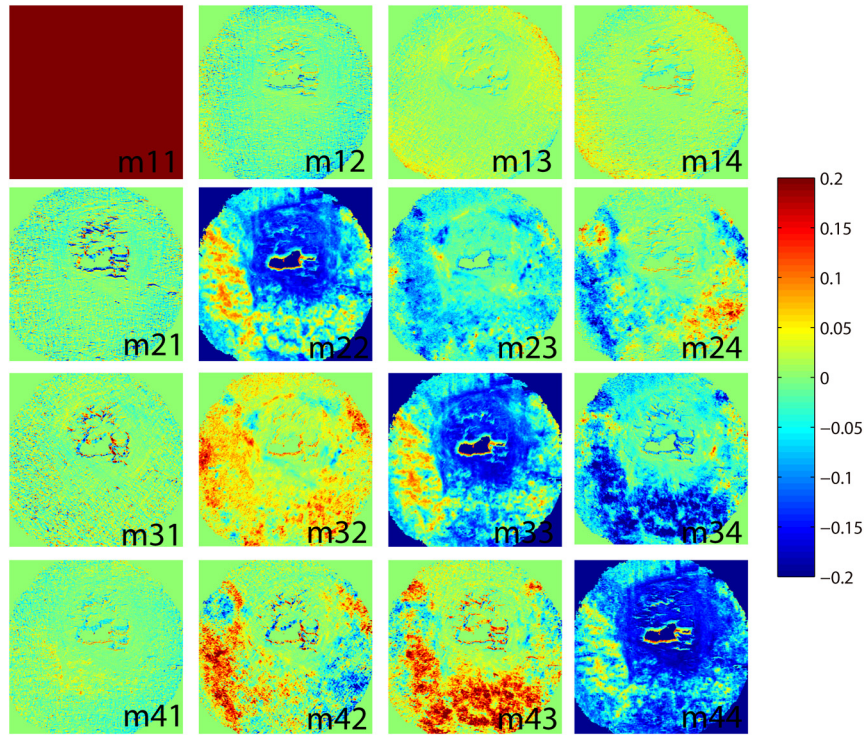
Fig. 7 Normalized backscattering Mueller matrix of the 28-μm thick non-stained paraffin slices of the human PTC tissue shown in Fig. 3(a). All the Mueller matrix elements are normalized by the m11. The color codes are from 0 to 1 for the m11, m22, m33, m44 elements and −0.2 to 0.2 for other elements.

parameters LDOP, b, A, D, Δ, and δ, as shown in Fig. 8. A pathology examination of these images reveals that the LDOP, MMT parameter b, MMPD parameters D, Δ, and δ do not display the cancerous region, but the image of parameter A clearly displays

a distinctive "abnormal" circular region of exceptionally higher values. It has been known from our previous studies that the parameter A is closely related to the "anisotropy" or degree of alignment of the fibrous structures.[18] It is also known in
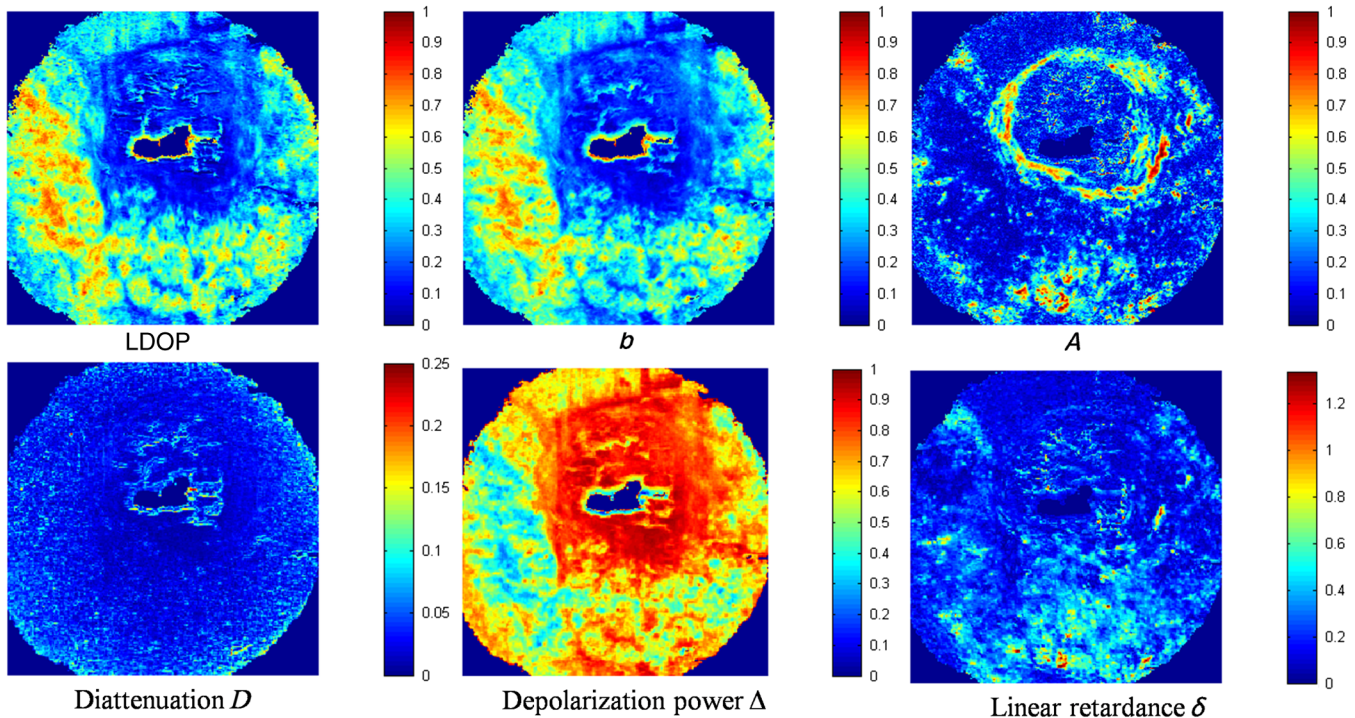

Fig. 8 Two-dimensional images of polarization parameters of the PTC tissue shown in Fig. 3(a): LDOP, MMT parameters b, A, MMPD parameters diattenuation D, depolarization power Δ, and linear retardance δ.
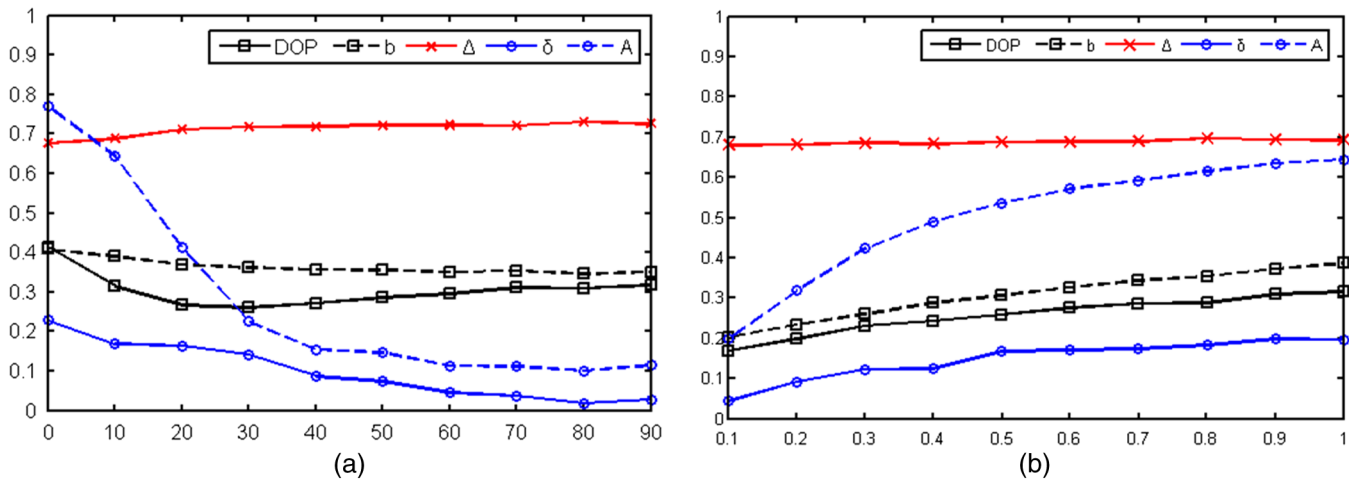
Fig. 9 Monte Carlo simulated dependence of parameters LDOP, b, Δ, δ and A to (a) the standard deviation of angular distribution of the cylinders (the order of alignment for the fibers), (b) the ratio between the scattering coefficients of cylinders and spheres.

clinical pathology that a distinctive feature of PTC is fibroplasias, which can be observed from the microscope image of Figs. 3(c) and 3(d) in the circular regions of the thyroid tissues. The tissues around the circular regions are pathologically identified as PCC. The experimental results clearly show that for the PTC tissues with fibrosis, the parameter A may serve as a sensitive indicator for clinical diagnosis.

Again, to examine the contrast mechanism for the polarization images of PTC, we conduct a Monte Carlo simulation based on the SCBM to show the relationship between the parameters (LDOP, b, Δ, δ, A) and the structures of fibrous tissues. To mimic structural features of fibroplasias, we can change the order of alignment of the fibrous scatterers by varying the standard deviation of their angular distributions and the volume fraction of the fibers by varying the ratio between the scattering coefficients of cylinders and spheres. In the scattering model for the PTC tissues, the spherical scatterers (4 μm in radius) represent the cell nuclei and the cylindrical scatterers (0.25 μm in radius) represent the fibers. The thickness of the medium is set to 28 μm. The refractive indices of the spherical and cylindrical scatterers are set to 1.45.[25,26] The refractive index of the ambient medium is 1.33. The total scattering coefficient of the cylindrical and spherical scatterers is 500 cm^{-1} according to Ref. 26. The simulated results in Fig. 9 show that as the microstructure of the sample becomes increasingly anisotropic by either decreasing the standard deviation of the angular distribution for the cylinders or increasing the volume fraction of the cylinders, the values of the parameter A sharply increase. The simulations confirm the experimental observation that the parameter A is a sensitive indicator for fibroplasias. The simulated results in Fig. 9 also indicate that the linear retardance δ should also respond to fibroplasias which were not observed in the experimental results (Fig. 8). This could be because the simulated values of the parameter A are always larger than that of the linear retardance δ. Also, it is known from other studies that δ is sensitive to other parameters of the scattering model such as the size of the cylindrical scatterers.[21] In summary, both the experiments and Monte Carlo simulations indicate that the parameter A is very sensitive to fibroplasias and may serve as an indicator for the clinical diagnosis of PTC.

4 Conclusion

In this paper, we apply backscattering polarization imaging technique on two types of cancerous tissues: human BCC and papillary thyroid carcinoma. Using the Mueller matrix elements, we calculate different polarization parameters: linear degree of polarization (LDOP), MMPD parameters diattenuation D, depolarization power Δ and linear retardance δ, and MMT parameters b and A, then use them to identify the characteristic features of the BCC and PTC cancerous tissues. A comparison between the backscattering polarization images of the 28-μm thick unstained slices and the histopathological analysis of the 4-μm H-E stained slices from the samples demonstrate that the polarization images reveal characteristic features of carcinomas. For the BCC samples, the parameters LDOP, D, Δ, and b exhibit contrast differences between the cancerous and normal tissues. For the PTC samples, the parameter A is the most sensitive to the existing cancerous tissues among these parameters. For better understanding, we conduct Monte Carlo simulations based on the SCBM to examine the relationship between the structural parameters of the scattering models, which correspond to morphological and pathological changes in cancerous tissues at the cellular level, and the characteristic features of the polarization parameters. The experimental and simulation results confirm that the parameters LDOP, Δ, and b are sensitive to the variations of "small" scatterers and the parameter A is sensitive to the alignment and volume fraction of the fibers in fibroplasias. This study reveals the contrast mechanisms for polarization imaging techniques of cancerous tissues and provides possibilities for future clinical applications.

References

1. V. Backman et al., "Detection of preinvasive cancer cells," *Nature* **406**(6791), 35–36 (2000).

2. M. H. Smith et al., "Mueller matrix imaging polarimetry in dermatology," *Proc. SPIE* **3911**, 210–216 (2000).
3. L. Qiu et al., "Multispectral scanning during endoscopy guides biopsy of dysplasia in Barrett's esophagus," *Nat. Med.* **16**(5), 603–606 (2010).
4. S. L. Jacques, J. R. Roman, and K. Lee, "Imaging superficial tissues with polarized light," *Lasers Surg. Med.* **26**(2), 119–129 (2000).
5. S. L. Jacques, J. C. R. Roman, and K. Lee, "Imaging skin pathology with polarized light," *J. Biomed. Opt.* **7**(3), 329–340 (2002).
6. S. L. Jacques et al., "Polarized light camera to guide surgical excision of skin cancers," *Proc. SPIE* **6842**, 684201 (2008).
7. A. Pierangelo et al., "Polarimetric imaging of uterine cervix: a case study," *Opt. Express* **21**(12), 14120–14130 (2013).
8. N. Zeng et al., "Linear polarization difference imaging and its potential applications," *Appl. Opt.* **48**(35), 6734–6739 (2009).
9. R. Liao et al., "Rotating linear polarization imaging for quantitative characterization of anisotropic tissues," *J. Biomed. Opt.* **15**(3), 036014 (2010).
10. R. Liao et al., "Penetration depth of linear polarization imaging for two-layer anisotropic samples," *Appl. Opt.* **50**(23), 4681–4687 (2011).
11. D. Z. Li et al., "Polarization imaging and scattering model of cancerous liver tissues," *J. Innov. Opt. Health Sci.* **6**(3), 1350025 (2013).
12. A. Pierangelo et al., "Ex-vivo characterization of human colon cancer by mueller polarimetric imaging," *Opt. Express* **19**(2), 1582–1593 (2011).
13. M. R. Antonelli et al., "Impact of model parameters on Monte Carlo simulations of backscattering Mueller matrix images of colon tissue," *Biomed. Opt. Express* **2**(7), 1836–1851 (2011).
14. T. Novikova et al., "The origins of polarimetric image contrast between healthy and cancerous human colon tissue," *Appl. Phys. Lett.* **102**(24), 241103 (2013).
15. S. Y. Lu and R. A. Chipman, "Interpretation of Mueller matrix based on polar decomposition," *J. Opt. Soc. Am. A* **13**(5), 1106–1113 (1996).
16. P. Shukla and A. Pradhan, "Mueller decomposition images for cervical tissue: potential for discriminating normal and dysplastic states," *Opt. Express* **17**(3), 1600–1609 (2009).
17. J. Chung et al., "Use of polar decomposition for the diagnosis of oral precancer," *Appl. Opt.* **46**(15), 3038–3045 (2007).
18. H. H. He et al., "A possible quantitative Mueller matrix transformation technique for anisotropic scattering media," *Photonics Lasers Med.* **2**(2), 129–137 (2013).
19. T. L. Yun et al., "Monte Carlo simulation of polarized photon scattering in anisotropic media," *Opt. Express* **17**(19), 16591–16602 (2009).
20. E. Du et al., "Two-dimensional backscattering Mueller matrix of sphere-cylinder birefringence media," *J. Biomed. Opt.* **17**(12), 126016 (2012).
21. Y. H. Guo et al., "A study on forward scattering Mueller matrix decomposition in anisotropic medium," *Opt. Express* **21**(15), 18361–18370 (2013).
22. H. H. He et al., "Two-dimensional and surface backscattering Mueller matrices of anisotropic sphere-cylinder scattering media: a quantitative study of influence from fibrous scatterers," *J. Biomed. Opt.* **18**(4), 046002 (2013).
23. T. Maeda et al., "Monte Carlo simulation of spectral reflectance using a multilayered skin tissue model," *Opt. Rev.* **17**(3), 223–229 (2010).
24. M. H. Sun et al., "Probing microstructural information of anisotropic scattering media using rotation-independent polarization parameters," *Appl. Opt.* **53**(14), 2949–2955 (2014).
25. V. V. Tuchin, L. V. Wang, and D. A. Zimnyakov, "Optical polarization in biomedical applications," Chapter 2 in *Tissue Structure and Optical Models*, E. Greenbaum, Ed., pp. 9–20, Oak Ridge National Laboratory, Oak Ridge, Tennessee (2006).
26. D. Hidovíc-Rowe and E. Claridge, "Modeling and validation of spectral reflectance for the colon," *Phys. Med. Biol.* **50**(6), 1071–1093 (2005).

Biographies of the authors are not available.